Lab on a Chip

PAPER

Cite this: *Lab Chip*, 2020, **20**, 2218

Remotely tunable microfluidic platform driven by nanomaterial-mediated on-demand photothermal pumping†

Guanglei Fu, ‡[ab] Wan Zhou ‡[a] and XiuJun Li *[acde]

Received 29th March 2020,
Accepted 14th May 2020

DOI: 10.1039/d0lc00317d

rsc.li/loc

The requirement of on-demand microfluidic pumps and instrument-free readout methods remains a major challenge for the development of microfluidics. Herein, a new type of microfluidic platform, an on-demand photothermal microfluidic pumping platform, has been developed using an on-chip nanomaterial-mediated photothermal effect as novel and remotely tunable microfluidic driving force. The photothermal microfluidic pumping performance can be adjusted remotely by tuning the irradiation parameters, without changing on-chip parameters or replacing enzymes or other reagents. In contrast to graphene oxide, Prussian blue nanoparticles with higher photothermal conversion efficiency were used as the model photothermal agent to demonstrate the proof of concept. The on-chip pumping distance is linearly correlated with both the irradiation time and the nanomaterial concentration. The applications of photothermal microfluidic pumping have been demonstrated in multiplexed on-chip transport of substances, such as gold nanoparticles, and visual quantitative bar-chart detection of cancer biomarkers without using specialized instruments. Upon contact-free irradiation using a laser pointer, a strong on-chip nanomaterial-mediated photothermal effect can serve as a robust and remotely tunable microfluidic pump in a PMMA/PDMS hybrid bar-chart chip to drive ink bars in a visual quantitative readout fashion. This is the first report on a photothermal microfluidic pumping platform, which has great potential for various microfluidic applications.

Introduction

Microfluidics has emerged as an increasingly attractive technology for point-of-care testing (POCT), especially in the fields of medical diagnostics, food and drug safety inspection, and environmental surveillance,[1–6] because of its outstanding merits of affordability, simplicity, portability, and high-throughput measurements.[7–13] Despite great research progress in microfluidics after more than two decades of development,[14–16] microfluidic platforms are still confronted with several major challenges.[17] In particular, the requirement of external microfluidic pumping accessories, such as pneumatic syringe pumps, usually results in higher cost, additional space, and operational complexity.[7,17] Additionally, the assay readouts of these microfluidic chips usually rely on bulky and costly instruments and detectors, such as fluorescence microscopes, electrochemical working stations, and microplate readers.[18,19] All these pumping and detection accessories have significantly compromised the inherent advantages of high portability and integrability and low cost of microfluidic systems.

Among various microfluidic analytical devices, volumetric bar-chart chips (V-Chips) have attracted great research attention particularly for quantitative POCT.[17,20–23] One of the most promising features of these V-Chips is that the assay results can be quantitatively displayed as visual bar charts without the aid of complex analytical instruments.[17,22] Based on the volumetric measurements of enzyme- or nanoparticle-catalyzed gas (*e.g.* O_2) production that acts as the microfluidic pump of the dye movement, different types of V-Chips have been developed for the quantitative detection of various disease biomarkers and pathogens.[20,24–26] However, several limitations are usually encountered in these V-Chips, such as relatively low operational stability because of inevitable denaturation of enzymes, dependence of the catalytic activity on surrounding environments, and

[a] *Department of Chemistry and Biochemistry, University of Texas at El Paso, 500 West University Ave, El Paso, Texas, 79968, USA. E-mail: xli4@utep.edu*
[b] *Biomedical Engineering Research Center, Medical School of Ningbo University, Ningbo, Zhejiang, 315211, P. R. China*
[c] *Biomedical Engineering, University of Texas at El Paso, 500 West University Ave, El Paso, Texas, 79968, USA*
[d] *Border Biomedical Research Center, University of Texas at El Paso, 500 West University Ave, El Paso, Texas, 79968, USA*
[e] *Environmental Science and Engineering, University of Texas at El Paso, 500 West University Ave, El Paso, Texas, 79968, USA*

† Electronic supplementary information (ESI) available: Details of the chip designs and the platform setup. See DOI: 10.1039/d0lc00317d

‡ These authors contributed equally to this work.

imprecise spatiotemporal controllability due to the intrinsic properties of the enzyme- or nanoparticle-catalyzed reactions.[23] Therefore, more robust, stable, on-demand, adjustable, and multiplexed microfluidic pumping systems are highly needed to be integrated into bar-chart chips.

The integration of classic physical principles in microfluidics has provided new possibilities for developing novel microfluidic platforms.[22] Nanomaterial-mediated photothermal effects have been the subject of intensive research due to the unique light-to-heat photophysical conversion property.[27–29] Currently, the near-infrared (NIR) laser-driven photothermal effect has been widely applied for photothermal therapy of cancers.[27,30–34] A number of nanomaterials that can convert NIR light into heat have been developed as photothermal agents, such as carbon-, gold- and Prussian blue (PB)-based nanomaterials.[27,35–41] Significantly, by using a portable laser pointer as a light source with remotely tunable irradiation parameters, rapid and substantial heat production can be simply achieved as a result of the nanomaterial-mediated photothermal effect,[40] making it particularly promising for the development of new point-of-care bioassays using a thermometer as a signal reader,[40–42] or serving as novel on-demand microfluidic driving force. Our group has originated multiple nanomaterial-mediated photothermal immunosensing systems for quantitative biochemical analysis.[40,41,43] However, to the best of our knowledge, the nanomaterial-mediated photothermal effect has not been exploited in microfluidic pumping, especially in bar-chart chips.

Herein, we developed a new type of microfluidic pumping platform, a tunable on-demand photothermal microfluidic pumping platform, using the on-chip nanomaterial-mediated photothermal effect as the new microfluidic driving force. The nanomaterial-mediated photothermal effect was explored as the microfluidic pump in a PMMA/PDMS (poly(methyl methacrylate)/polydimethylsiloxane) hybrid photothermal bar-chart chip (PT-Chip) to propel on-chip ink-bar-chart movement in a visual quantitative readout fashion, as shown in Scheme 1A. Two types of photothermal agents, PB NPs and graphene oxide (GO), were used to study the feasibility of the photothermal microfluidic pump. Upon the contact-free irradiation of the nanomaterial suspensions on the PT-Chip with an 808 nm laser, the on-chip photothermal effect results in rapid and substantial heat production. The subsequent heating of solutions leads to the rapid accumulation of vapor pressure in limited volumes of the inlets, thereby pumping the on-chip visual bar-chart movement of the nanomaterial suspensions. On-chip photothermal effects of the nanomaterials were investigated in three PT-Chips (Fig. S1 and S2†) to demonstrate the proof of concept of the photothermal microfluidic pumping platform. Furthermore, we have exemplified its application for multiplexed on-chip transport of substances, such as gold nanoparticles (AuNPs) as shown in Scheme 1B, and visual quantitative readout of immunoassay signals in the photothermal bar-chart chip. To the best of our knowledge, this is the first attempt to exploit the nanomaterial-mediated photothermal effect for microfluidic pumping and also serves as the first report on a photothermal bar-chart microfluidic pumping platform, with potential for various microfluidic applications, especially for visual quantitative POCT.

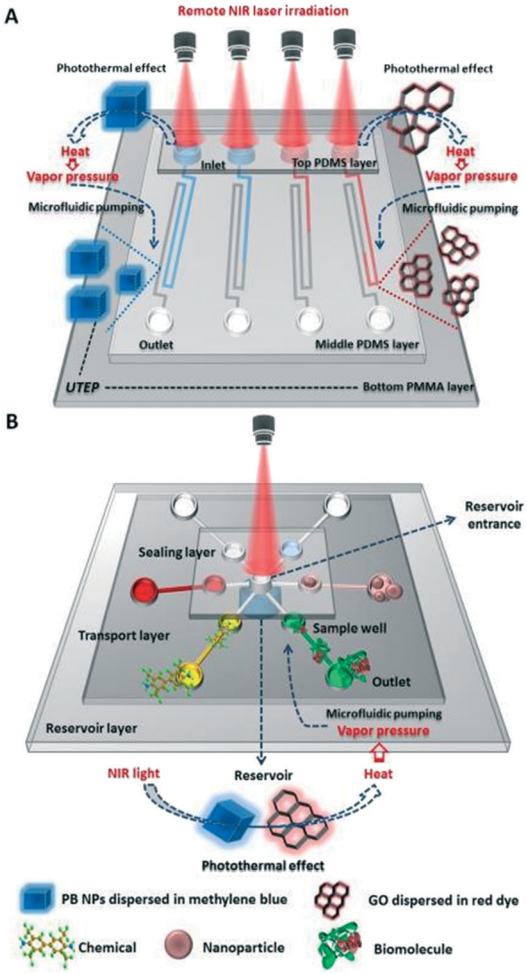

Scheme 1 Schematic illustration of (A) the photothermal microfluidic bar-chart chip using the on-chip nanomaterial-mediated photothermal effect as the microfluidic driving force and (B) multiplexed on-chip transport of substances using the photothermal microfluidic pumping.

Results and discussion

Off-chip investigation on the photothermal effects of the nanomaterials

As a new generation of NIR laser-driven photothermal agents with high photothermal conversion efficiency,[35] PB NPs were herein selected as a model photothermal agent in contrast to a typical kind of photothermal agent, GO.[44,45] In comparison with methylene blue (MB) and red food dye (RD) as blank dye indicators, the off-chip photothermal effects of the nanomaterials in the presence of dye indicators were investigated before the on-chip photothermal study. UV-vis absorption spectrometry was utilized to characterize the optical absorption properties of the nanomaterials in the NIR region as

shown in Fig. 1. Typically, a broad absorption band from 450 nm to 900 nm was observed in the UV-vis absorption spectra of PB NPs with a strong absorption peak at 715 nm, which can be attributed to the charge transfer transition between Fe(II) and Fe(III) in PB NPs.[35,46] Strong optical absorption of PB NPs in the NIR region after 800 nm was still observed, whereas both MB and RD showed no apparent absorption after 750 nm. As a classic kind of carbon-based photothermal agent, GO also exhibited distinct optical absorption in the NIR region but with significantly lower absorbance than PB NPs at the same concentration. The molar extinction coefficient of PB NPs at 808 nm (1.09×10^9 M^{-1} cm^{-1}) was reported to be several orders of magnitude higher than that of carbon-based nanomaterials (7.90×10^6 M^{-1} cm^{-1}).[35]

To further confirm the photothermal effect of the nanomaterials and study the effect of the dye indicators (*i.e.* MB and RD) on the photothermal responses, the off-chip photothermal effects of the nanomaterials in the presence of the dye indicators were investigated by employing an 808 nm diode laser as the NIR light source. Fig. 2A and B show the temperature changes of the nanomaterial suspensions and the blank dye solutions during the horizontal laser irradiation process for 10 min. A digital thermometer was inserted into the suspensions to record the temperature. As expected, both PB NP and GO suspensions exhibited dramatic temperature increases in a concentration-dependent manner during the irradiation process, whereas only minor temperature increases of less than 2.0 °C were observed from the blank dye solutions. The results indicated the intrinsically poor NIR laser-driven photothermal effect of MB and RD owing to their weak optical absorption in the NIR region as demonstrated in Fig. 1. PB NPs at a low concentration of 0.01 mg mL^{-1} resulted in a drastic temperature elevation of 10.5 °C after the irradiation. Irradiation of the PB NP suspension at a concentration of

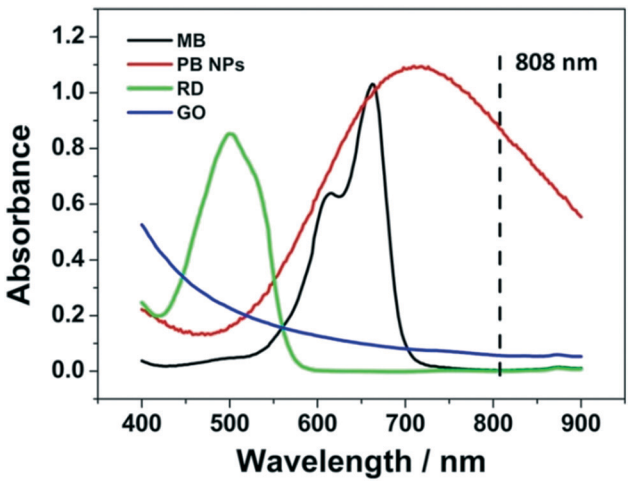

Fig. 1 Optical absorption properties of the nanomaterials and dye indicators in the NIR region. UV-vis absorption spectra of methylene blue (MB, 0.0125 mg mL^{-1}), red food dye (RD), PB NP (0.1 mg mL^{-1}) and GO (0.1 mg mL^{-1}) aqueous suspensions.

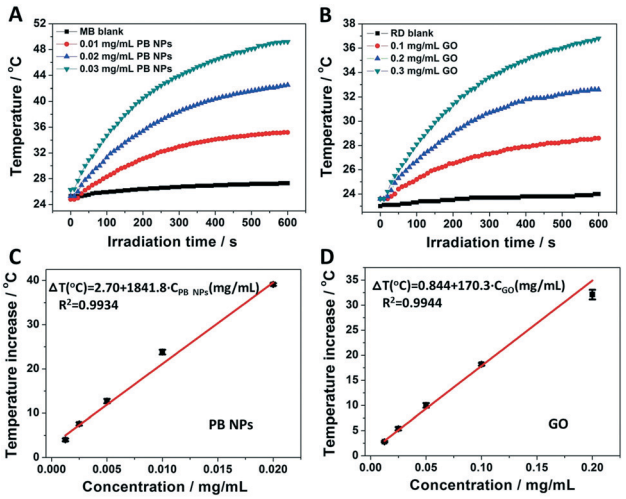

Fig. 2 Off-chip photothermal effect-induced temperature elevation of the nanomaterials and dyes as a function of (A and B) irradiation time and (C and D) nanomaterial concentration. Temperature comparison among (A) different concentrations of PB NPs suspended in MB solutions (0.054 mg mL^{-1}) and (B) different concentrations of GO suspended in RD solutions during the laser irradiation process for 10 min at a power density of 3.12 W cm^{-2}. Temperature increases (ΔT) *vs.* concentrations of (C) PB NP suspensions and (D) GO suspensions after the laser irradiation for 1.0 min at a power density of 5.26 W cm^{-2}. Error bars represent the standard deviations (n = 4).

0.03 mg mL^{-1} for only 1.0 min led to a rapid temperature increase of 5.5 °C. In contrast to PB NPs, GO with a 10-fold higher concentration exhibited a much slower temperature elevation rate than PB NPs at each concentration, suggesting a stronger NIR laser-driven photothermal effect of PB NPs than that of GO because of the higher molar extinction coefficient of PB NPs at 808 nm.

To investigate the relationship between the photothermal effect-induced temperature elevation and the nanomaterial concentration, the nanomaterial suspensions at different concentrations were vertically exposed to the 808 nm laser for 1.0 min. The temperature of the suspensions was immediately recorded by using a digital thermometer after the irradiation. Fig. 2C and D show the temperature increment as a function of the nanomaterial concentration. It was found that the temperature elevation values of both PB NP and GO suspensions were proportional to the nanomaterial concentrations in the ranges of 0.00125–0.02 mg mL^{-1} and 0.0125–0.2 mg mL^{-1}, respectively. It was worth noting that PB NPs exhibited a 10.8-fold higher slope than GO, further demonstrating the stronger photothermal effect of PB NPs than that of GO.[35]

On-chip photothermal effects of the nanomaterials

By utilizing MB and RD as the on-chip dye indicators of PB NPs and GO, respectively, the on-chip photothermal effects of the nanomaterials were investigated in a PMMA/PDMS hybrid microfluidic chip (see chip 1 in Fig. S1†). The nanomaterials were suspended in the dye solutions and then loaded into the

inlets of the PT-Chip, followed by sealing of the inlets with a top PDMS layer. Hence, chip 1 preloaded with the nanomaterial–dye suspensions was assembled with only the outlets accessible to the atmosphere. To study the photothermal microfluidic pumping performance of the PT-Chip, the inlets of chip 1 were individually exposed to the laser using blank MB and RD as controls. The photothermal pumping distance of the dye indicators was quantitatively measured by using a visual on-chip ruler. As shown in Fig. 3, both PB NPs (channel 2) and GO (channel 4) displayed rapid and visual on-chip bar-chart pumping of the nanomaterial–dye suspensions after the laser irradiation for 50 s (see the ESI† for the recorded video), whereas MB (channel 1) and RD (channel 3) displayed no apparent bar-chart movement due to their poor photothermal effects. GO with a 10-fold higher concentration showed a 3.0-fold shorter bar-chart movement distance than PB NPs, which can be attributed to the weaker photothermal effect of GO than that of PB NPs, as demonstrated in Fig. 2. In contrast, PB NPs at a low concentration of 0.1 mg mL^{-1} still resulted in a bar-chart pumping distance of 64.4 mm under the irradiation process for only 50 s, thus suggesting the robustness of the photothermal effect as the bar-chart microfluidic driving force.

During the irradiation process of the nanomaterial–dye suspensions, the on-chip nanomaterial-mediated photothermal effect resulted in rapid and substantial heat production in the inlets. The subsequent heating of solutions led to the rapid accumulation of vapor pressure inside the inlets with limited volumes, thereby driving the visual bar-chart movement of the nanomaterial–dye suspensions in the channels. Therefore, a new type of bar-chart microfluidic platform, the photothermal bar-chart chip (PT-Chip), was developed using the on-chip nanomaterial-mediated photothermal effect as the microfluidic driving force, as illustrated in Scheme 1A. In addition to the robustness of the photothermal microfluidic pump, another key feature of the new PT-Chip is that the on-chip photothermal pumping rate is highly tunable by remotely adjusting the parameters of the laser, whereas it is quite challenging to spatiotemporally adjust enzyme- or nanoparticle-catalyzed reactions on a chip. It was observed that the ongoing bar-chart movement can be instantly terminated upon the removal of the laser irradiation. It should be noted that the nanomaterial-mediated photothermal effect is more stable than the enzyme-catalyzed gas-production approach as a microfluidic photothermal pump, because enzymes can easily lose activity at room temperature while photophysical conversion efficiency is intrinsically inert to surrounding environments. Furthermore, by tuning the irradiation diameter of the laser spot and changing the layout of the chip, multiple inlets can be irradiated at one irradiation process, enabling on-demand microfluidic pumping in a multiplexed manner. These results indicated the feasibility of utilizing the on-chip nanomaterial-mediated photothermal effect as a new type of robust, tunable, and versatile microfluidic driving force in bar-chart chips.

We further systematically studied other fundamental aspects of the PT-Chip. To study the influence of irradiation time on the performance of the PT-Chip, the inlets of chip 1 loaded with the same concentrations of the nanomaterial–dye suspensions were individually irradiated with the laser for different times. As shown in Fig. 4, with the increase of the irradiation time, gradually longer bar-chart movement distance was clearly observed in both cases of PB NPs and

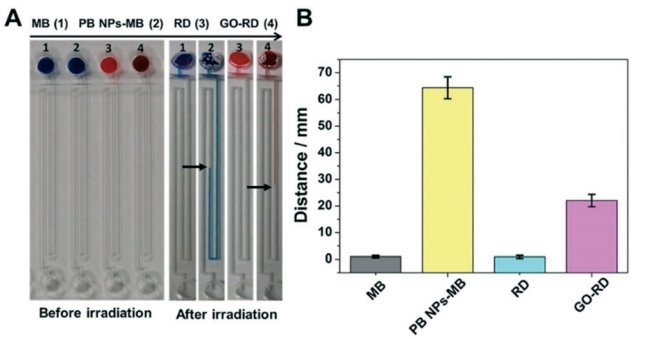

Fig. 3 On-chip photothermal microfluidic pumping performance of the PT-Chip (chip 1). (A) Photographs of the PT-Chip loaded with blank MB, PB NP–MB (0.1 mg mL^{-1}), blank RD, and GO–RD (1.0 mg mL^{-1}) suspensions before and after the laser irradiation for 50 s at a power density of 2.6 W cm^{-2}. The black arrows indicate the endpoint of the dye bars. (B) Comparison among on-chip photothermal pumping distances after the laser irradiation. Error bars represent the standard deviations (n = 4).

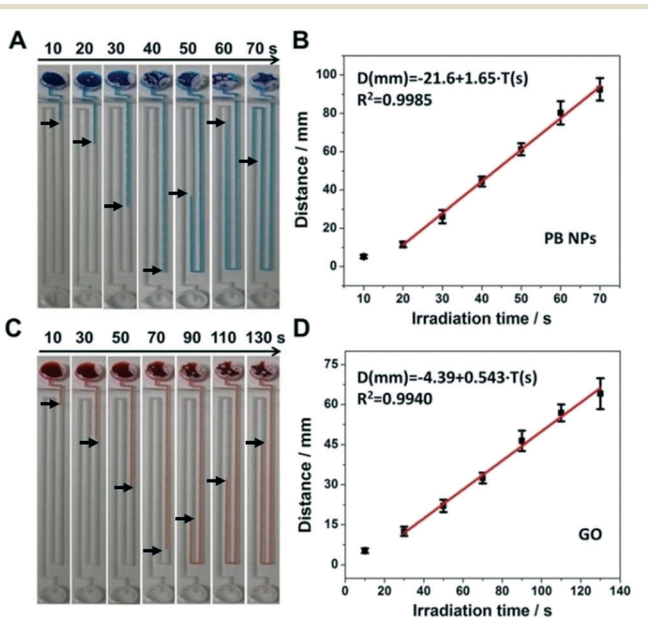

Fig. 4 Effect of laser irradiation time on the photothermal microfluidic pumping performance of the PT-Chip (chip 1). (A) Photographs of the PT-Chip loaded with PB NP–MB suspensions (0.1 mg mL^{-1}) after the laser irradiation for different times at 2.6 W cm^{-2}. (B) On-chip photothermal pumping distance of the PB NP–MB suspensions as a function of the irradiation time. (C) Photographs of the PT-Chip loaded with GO–RD suspensions (1.0 mg mL^{-1}) after the laser irradiation for different times. (D) Photothermal pumping distance of the GO–RD suspensions as a function of the irradiation time. The black arrows indicate the endpoint of the dye bars. Error bars represent the standard deviations (n = 4).

GO. Longer irradiation time of the nanomaterials caused increasing amounts of on-chip generated heat, consequently leading to the progressive accumulation of increasing vapor pressure in the limited volumes of the inlets. In good agreement with the result obtained in Fig. 3, PB NPs with a 10-fold lower concentration displayed a longer bar-chart pumping distance than GO for each irradiation time. Both PB NPs and GO showed a good linear relationship between the photothermal pumping distance and the irradiation time in the ranges of 10–70 s and 10–130 s, respectively. Significantly, PB NPs exhibited a 3.0-fold higher slope than GO, implying the higher photothermal microfluidic pumping efficiency of PB NP-mediated photothermal effect than that of GO.

In addition, the effect of the nanomaterial concentration on the performance of the PT-Chip was investigated, as shown in Fig. 5. Inlets preloaded with different concentrations of the nanomaterial–dye suspensions were individually irradiated for the same time. With the increase of the nanomaterial concentration, PB NPs displayed an increasingly longer bar-chart pumping distance that was obviously longer than GO even with 10-fold higher concentrations and longer irradiation times. Higher concentrations of the nanomaterials accordingly led to the accumulation of higher vapor pressure in the inlets as a result of the concentration-dependent photothermal effect of the nanomaterials. The bar-chart pumping distances of both PB NPs- and GO-driven PT-Chips were proportional to the concentrations of the nanomaterials in the ranges of 0.00625–0.2 mg mL^{-1} and 0.0625–2.0 mg mL^{-1}, respectively, which laid the basis for the quantitative application of the PT-Chips. The quantitative readout results of the microfluidic pumping performance are visually displayed as on-chip ink-bar-charts without the aid of any complex and costly analytical instruments, making it particularly advantageous for POCT.

To evaluate the reproducibility of the photothermal microfluidic pumping performance, the inlets of chip 1 preloaded with the same concentrations of the nanomaterials were individually irradiated for the same time. As shown in Fig. 6, the PT-Chips driven by both PB NPs- and GO-mediated photothermal effects displayed uniform bar-chart movement distance after the irradiation. Measurements of the bar-chart pumping distance of the six parallel inlets loaded with PB NPs and GO showed low relative standard deviations (RSDs) of 4.6% and 5.1%, respectively, indicating the good reproducibility of the photothermal bar-chart microfluidic pumping performance of the PT-Chip.

Application in multiplexed on-chip transport of substances using the photothermal microfluidic pump

It has been well established that on-chip transport of fluids or substances, such as nanoparticles and chemicals, is of

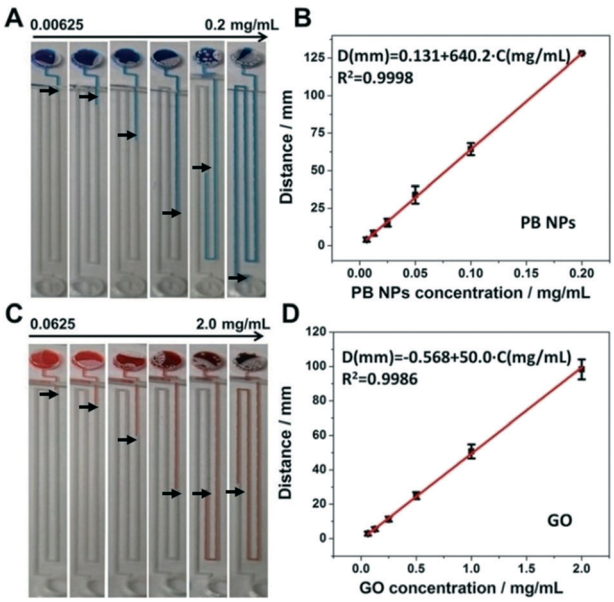

Fig. 5 Effect of the nanomaterial concentration on the photothermal bar-chart microfluidic pumping performance of the PT-Chip (chip 1). (A) Photographs of the PT-Chip loaded with different concentrations of PB NP–MB suspensions after the laser irradiation for 50 s at 2.6 W cm^{-2}. (B) Calibration plot of the bar-chart pumping distance of the PB NP–MB suspensions *vs.* PB NP concentration. (C) Photographs of the PT-Chip loaded with different concentrations of GO–RD suspensions after the laser irradiation for 90 s. (D) Calibration plot of the bar-chart pumping distance of the GO–RD suspensions *vs.* GO concentration. The black arrows indicate the endpoint of the dye bars. Error bars represent the standard deviations (n = 4).

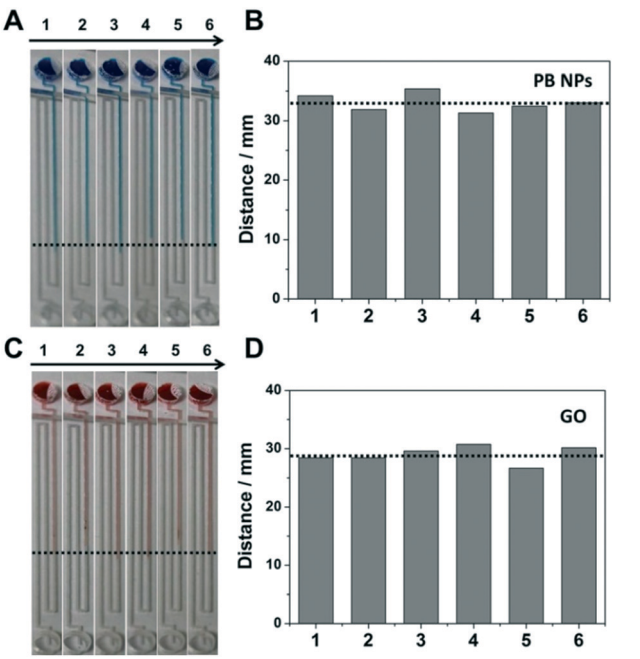

Fig. 6 Reproducibility of the photothermal microfluidic pumping performance of the PT-Chip. (A) Photographs and (B) the measured bar-chart pumping distance of chip 1 loaded with the same concentration of PB NP–MB suspensions (0.05 mg mL^{-1}) after the laser irradiation for 50 s at 2.6 W cm^{-2}. (C) Photographs and (D) the measured bar-chart pumping distance of chip 1 loaded with the same concentration of GO–RD suspensions (0.5 mg mL^{-1}) after the laser irradiation for 90 s.

significant importance for various microfluidic applications.[47–49] Dye transport driven by different pumping principles is the foundation of bar-chart chips.[20] To further exemplify the application of the photothermal microfluidic pumping system, on-chip transport of substances, such as dyes and AuNPs, using two PT-Chips (see chip 2 and chip 3 in Fig. S1 and S2†) was conducted employing the photothermal microfluidic pumps.

On-chip single-sample transport upon one laser irradiation process was first performed using a new microfluidic PT-Chip (chip 2) as a proof of concept. PB NP suspensions were preloaded in the reservoirs of chip 2 and the target substances were stored in middle sample wells as shown in Fig. 7A. To assess the possibility of the PT-Chip for on-chip transport of nanoparticles, a AuNP-catalyzed TMB–H_2O_2 colorimetric reaction system was integrated on the PT-Chip. Herein, AuNPs were stored in the sample wells with preloaded TMB–H_2O_2 solutions in the outlets. Owing to the AuNP-catalyzed TMB–H_2O_2 colorimetric reaction,[50–52] the successful pumping of AuNPs to the outlets can result in visual color changes from colorless to blue. To prevent the mixing of PB NPs with the target transport substances during the irradiation, PB NP suspensions were loaded below the reservoir entrances in the third layer (*i.e.* the PMMA plate). Insets in Fig. 7A show the PT-Chip (chip 2) before and after the laser irradiation of each reservoir. Upon individual irradiation of the reservoirs, dyes stored in the sample wells were pumped rapidly to the outlets through the channels, thereby displaying the corresponding color changes in the outlets. Interestingly, a clear color change from colorless to blue was also observed in the outlet loaded with TMB and H_2O_2, suggesting the successful pumping of AuNPs from the sample well to the outlet where the AuNP-catalyzed TMB–H_2O_2 colorimetric reaction took place.[50–52] A significantly high flow rate of 1.8 mm s^{-1} was achieved at a low PB NP concentration of 0.1 mg mL^{-1}. It was found that the bar-chart flow rate was positively correlated with the PB NP concentration in the range from 0.025 to 0.8 mg mL^{-1}. With the increase of the PB NP concentration, increasing PB NPs-mediated photothermal effect led to the increasing vapor pressure in the reservoirs. The pressure pathway extended from the reservoir entrances to the sample wells, thus pumping the target substances to move towards the outlets. These results demonstrated the successful application of the PB NP-mediated photothermal effect as the photothermal microfluidic pump for on-chip transport of substances.

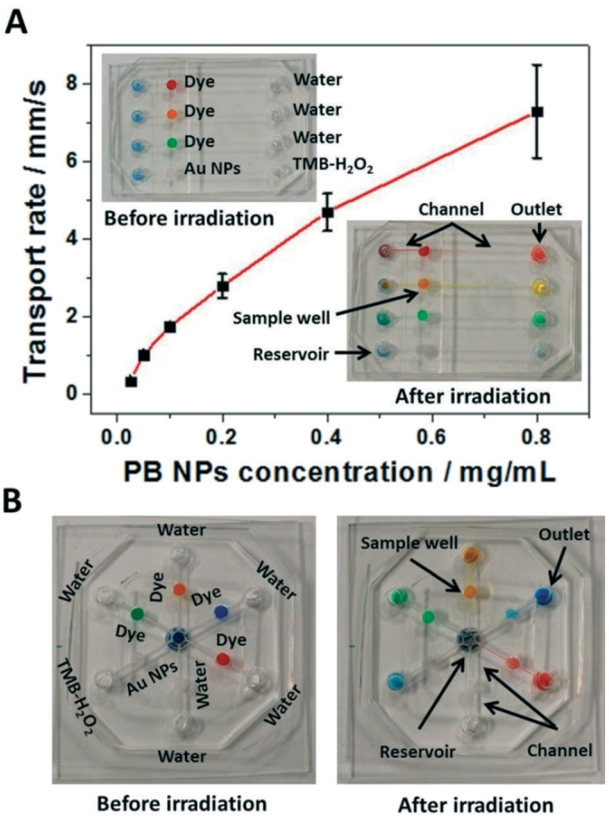

Fig. 7 Application of the photothermal microfluidic pump for on-chip transport of dyes and AuNPs. (A) On-chip transport rate as a function of PB NP concentrations in the single-sample transport PT-Chip (chip 2). Insets: photographs of chip 2 before and after the laser irradiation (2.6 W cm^{-2}) at a PB NP concentration of 0.1 mg mL^{-1}. (B) Photographs of the multiplexed transport PT-Chip (chip 3) before and after the laser irradiation at a PB NP concentration of 0.4 mg mL^{-1}. Error bars represent the standard deviations (n = 4).

To further verify the possibility of the PT-Chip for on-chip transport of substances in a multiplexed manner, a new multiplexed PT-Chip (chip 3) was fabricated, as shown in Fig. 7B. On this multiplexed photothermal microfluidic pumping system, one central reservoir was connected to multiple pumping pathways and sample wells through the reservoir entrance. PB NP suspensions (80 μL, 0.4 mg mL^{-1}) were loaded into the central reservoir, while the dyes and AuNPs (20 μL per sample well) were independently stored in six sample wells. Surprisingly, upon only one irradiation process for 2.0 min of the central reservoir, the dyes and AuNP suspensions in all sample wells were simultaneously pumped into relevant outlets with a rapid pumping rate of 60 μL min^{-1}. Hence, the PB NP-mediated photothermal effect achieved from only one central reservoir was sufficient to pump at least six microfluidic pathways, demonstrating great potential of the PB NP-mediated photothermal effect for on-chip sample transport in a multiplexed manner. Similarly, as discussed in the results in Fig. 3, the on-chip transport process can be immediately terminated upon the removal of the laser irradiation. The transport rate is also highly controllable by remotely adjusting the parameters of the laser. It is cumbersome to change enzyme concentrations to control the catalytic reaction rate for gas production on a highly integrated chip. Furthermore, it is worth noting that contamination and denaturation of target samples can be effectively avoided during the on-chip transport process, since target samples are well separated from the photothermal nanomaterials in the central reservoir where only vapor pressure travels outside the reservoir through the reservoir entrance. Thus, the target samples are neither contaminated nor heated during the transport process, which

is of appealing advantage for on-chip multiplexed transport of biomolecules, such as protein and DNA. In addition, both PB NPs and GO used in the PT-Chips are typical NIR laser-driven photothermal nanomaterials with simple preparation, low cost, low cytotoxicity, and synthetically modifiable photothermal properties (*e.g.* particle size, material shape, and surface modification), making them practically adaptable for extensive applications in the PT-Chips. Since the particle size can affect the photothermal effects, the photothermal effects of different-sized nanomaterials can be further optimized to achieve desired pumping performance.

Application in visual quantitative biochemical analysis using the photothermal microfluidic bar-chart platform

To further extend the application of the photothermal bar-chart microfluidic pumping platform in visual quantitative biochemical analysis, we applied our PT-Chip for the visual quantitative detection of a prostate-specific antigen (PSA, a prostate cancer biomarker) based on the readout of the photothermal pump-driven movement distance of the ink bars, without using specialized instruments. As illustrated in Fig. 8A, iron oxide NPs conjugated with a detection antibody (*i.e.* anti-PSA antibody) were used to bridge a sandwich-type immunoassay with the photothermal sensing strategy according to our previous studies.[40,41] Since the photothermal effect of captured iron oxide nanoparticles was too weak, they were converted into a strong photothermal agent, PB NPs. After the conversion, the immunosensing solutions obtained from the different concentrations of the target PSA were loaded into the multiple inlets of the PT-Chips, which were irradiated simultaneously by one NIR laser beam. Different amounts of PB NPs produced from the immunoassay with varying concentrations of the PSA led to the on-chip generation of different amounts of heat and corresponding bar-chart pumping distances as the visual quantitative readout signals. As shown in Fig. 8B, one channel with 64 ng mL^{-1} PSA displayed a bar-chart pumping distance of 20.9 mm, while the control channel (*i.e.* 0 ng mL^{-1} PSA, blank) only exhibited a negligible pumping distance. It is worthy to note that the bar-chart pumping distance was proportional to the concentration of the PSA in the range from 2 ng mL^{-1} to 64 ng mL^{-1} upon the laser irradiation for 5 min at a power density of 2.2 W cm^{-2}. The limit of detection (LOD) was determined to be 2.0 ng mL^{-1} based on the signal-to-noise ratio of three, which indicated the high sensitivity and capability of the PT-Chip to meet the cut-off requirement of clinical diagnostics using 4.0 ng mL^{-1} as the threshold concentration.[34,47] The results exemplified a new application of the nanomaterial-mediated photothermal microfluidic pumping platform, and demonstrated the excellent performance of the PT-Chip for visual quantitative readout of bioassay signals, with no aid of any bulky and expensive analytical instruments (even a thermometer[40,41]).

Herein, it should be noted that the off-chip PSA immunoassay only serves as a proof-of-concept study to prove the capability of the PT-Chip for the visual quantitative readout of detection signals using the photothermal pumping principle, since the development of the photothermal bar-chart pumping platform is the major focus of the work. On the basis of the present pumping platform, we believe that various photothermal agent-involved immunoassay systems can be integrated into the PT-Chip to enable the simple on-chip visual quantitative POCT,[53] owing to the superiority of the new microfluidic pumping platform.

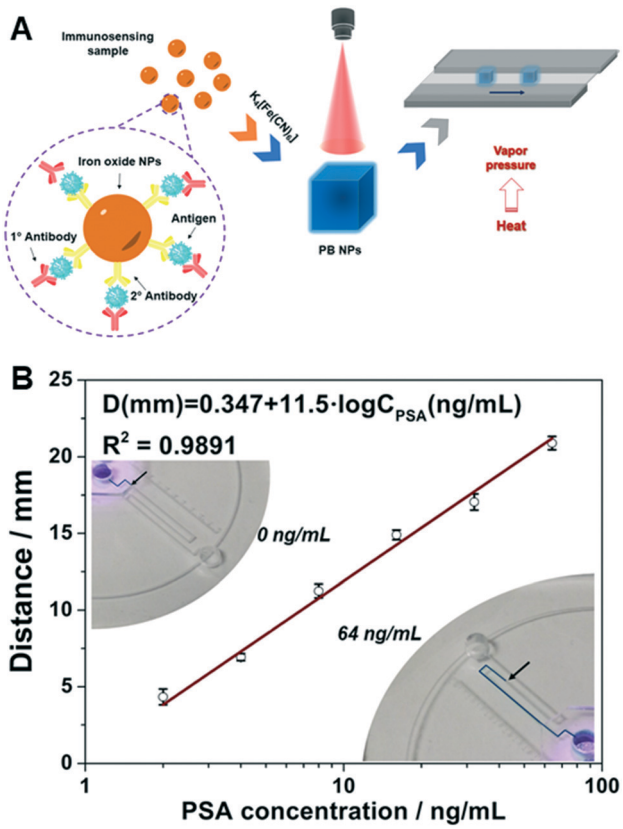

Fig. 8 Visual quantitative readout of PSA concentrations using a 4-channel PT-Chip. (A) Schematic illustration of the photothermal immunoassay including the off-chip iron oxide NP-involved immunoassay, the conversion from iron oxide NPs to PB NPs, and the on-chip visual quantitation based on the bar-chart pumping distances. (B) The calibration curve of the on-chip detection of PSA using the measured bar-chart pumping distance with different concentrations of PSA after the laser irradiation for 5 min at 2.2 W cm^{-2}. Insets: photographs taken during the on-chip detection of PSA at 0 and 64 ng mL^{-1}, respectively. Error bars represent the standard deviations (n = 4).

Conclusions

We developed a new type of microfluidic pumping platform, a photothermal microfluidic chip (PT-Chip), based on the integration of on-chip nanomaterial-mediated photothermal effect as novel on-demand microfluidic driving force. We designed 3 different chips to study different fundamental aspects and demonstrated the proof of concept of the tunable PT-Chip. The remotely tunable photothermal effect of nanomaterials propelled the robust on-chip bar-chart

movement of dyes, enabling visual quantitative readouts and the exploration of the on-chip nanomaterial-mediated photothermal effect as a new type of on-demand microfluidic pump. We further exemplified the application of the photothermal microfluidic pump for on-chip transport of substances, such as AuNPs, by using chip 2 and chip 3 in a multiplexed manner. This microfluidic photothermal pumping strategy was also applied for the visual quantitative detection of a cancer biomarker on the PT-Chip based on the visual readout of the bar-chart pumping distances, without using any specialized instruments. The LOD down to the concentration of 2.0 ng mL^{-1} PSA was achieved, meeting the sensitivity requirement in clinical diagnostics. In comparison with the traditional V-Chips using enzyme- or nanoparticle-catalyzed gas production as the driving force, the PT-Chip is particularly advantageous because of its robustness (*i.e.* high and rapid photothermal conversion efficiency), remote on-demand controllability (*i.e.* precise controllability by remotely adjusting the laser parameters), stability (*i.e.* inertness of the photophysical conversion efficiency to surrounding environments), and flexibility and versatility (*i.e.* applicability to a wide range of photothermal nanomaterials and small organic photothermal molecules). With the commercial availability of various affordable and powerful pen-style laser pointers, another key merit of the photothermal microfluidic pump is its portability by using a handheld laser pointer as the light source, compared with traditional pneumatic syringe pumps. Furthermore, unlike most traditional injector-based microfluidic pumping, no connecting accessories (*e.g.* injection syringes and tubes) are required for the PT-Chips, thus optimizing operational space and simplicity. Our chip's main advantages over conventional pumping lie in: 1) contact-free; 2) remotely tunable; 3) small size; 4) less complex; 5) reagent transport in "local" regions without affecting other sections; 6) a photothermal bar-chart chip for visual quantitative biochemical analysis without using any specialized instruments. As far as we know, this is the first report on a microfluidic pumping platform using the on-chip nanomaterial-mediated photothermal effect as the microfluidic driving force, which will have great potential for various microfluidic applications, particularly for the visual quantitative POCT of various biochemicals.

Experimental section

Materials and instruments

Poly(methyl methacrylate) (PMMA, 2.0 mm in thickness) sheets were purchased from McMaster-Carr (Los Angeles, CA). Polydimethylsiloxane (PDMS, Sylgard 184) was acquired from Dow Corning (Midland, MI). The graphene oxide (GO) nanosheets were the product of Graphene Laboratories (Calverton, NY). Methylene blue (MB) and prostate-specific antigen (PSA) were purchased from Sigma-Aldrich (St. Louis, MO). Red food dyes were obtained from Walmart (El Paso, TX). Prussian blue nanoparticles (PB NPs) were prepared according to the literature.[54,55] All solutions and nanomaterial suspensions were prepared with ultrapure Milli-Q water (18.2 MΩ cm) collected from a Milli-Q system (Bedford, MA). Unless otherwise stated, all other chemicals were of analytical grade and were used as received. UV-vis absorption spectroscopic characterization was carried out on a SpectraMax Multi-Mode Microplate Reader (Molecular Devices, LLC, Sunnyvale, CA) utilizing a 96-well microplate. The temperature of the suspensions was measured by using a digital thermometer (KT-300 LCD) with a detection range of −50 to +300 °C. An 808 nm diode laser (MDL-III-808) with an output power supply (PSU-III-LED) adjustable from 0 W to 2.5 W was obtained from Opto Engine LLC (Midvale, UT).

Design and fabrication of the PMMA/PDMS hybrid photothermal microfluidic chips

We designed three chips (see Fig. S1†) to demonstrate the versatile applications of the PT-Chips. Patterns of these chips were designed with the Adobe Illustrator CS5 software, followed by laser ablation of the PMMA/PDMS sheets by employing a laser cutter (Epilog Zing 16, Golden, CO). As shown in Fig. S1,† the PT-Chip (chip 1) was composed of three layers including a bottom PMMA plate (2.0 mm in thickness), a middle PDMS slice (4.0 mm in thickness), and a top PDMS sealing slice (2.0 mm in thickness). Channels with a width of 0.25 mm and inlets with a diameter of 3.0 mm were created on the bottom PMMA plate by employing the laser cutter. The fabrication parameters (*e.g.* speed : power intensity) for the channels and inlets were 40 : 40% and 25 : 50%, respectively. An on-chip ruler for the measurement of the bar-chart pumping distance was carved on the bottom PMMA plate. Inlets and outlets with a diameter of 3.0 mm were thoroughly punched in the middle PDMS slice by using a puncher (Harris, USA). Both PMMA plates and PDMS slices were thoroughly washed before the chip assembly, followed by treatment with a plasma cleaner (PDC-32 G) for 30 seconds. To fabricate the PMMA/PDMS hybrid microfluidic chips, the bottom PMMA plate with patterns facing up was coated with the middle PDMS slice. The two layers were aligned to overlap the corresponding wells. The nanomaterials (PB NPs and GO) were first suspended in aqueous solutions of the dyes (*i.e.* MB and RD) and then preloaded in the inlets (20 μL) of the chips. The inlets were ultimately sealed with the top PDMS slice.

Design and fabrication of the photothermal microfluidic transport chip

The single-sample transport chip (chip 2) was fabricated with five layers: 1) a bottom PMMA plate (2.0 mm in thickness) with superficially carved reservoirs and outlets facing up; 2) a PDMS slice (4.0 mm in thickness) as the second layer with thoroughly punched reservoirs and outlets; 3) another PMMA plate as the third layer with thoroughly carved outlets and reservoir entrances (3.0 mm in diameter) and superficially carved patterns with channels and sample wells facing up; 4) a PDMS slice (4.0 mm in thickness) with thoroughly punched sample

wells and outlets as the fourth layer; 5) another PDMS slice (2.0 mm in thickness) as the top sealing layer of the sample wells. All reservoirs and outlets had the same diameter of 6.0 mm. The diameter of all sample wells was 4.0 mm. The width of the channels on the PMMA plate (*i.e.* the third layer) was 0.25 mm. All layers were sequentially assembled together from bottom to top by aligning the corresponding wells. PB NP suspensions (40 μL per well) were injected into the reservoirs through the reservoir entrances after assembling the third layer. Target samples (20 μL), such as dyes and AuNPs, were preloaded in the sample wells after assembling the fourth layer. The multiplexed transport chip (chip 3) was fabricated according to the same protocol as mentioned above, except the major difference that one central reservoir was shared with six channels in this chip. Six sample wells were connected to one central reservoir entrance.

Off-chip and on-chip investigation of photothermal effects of nanomaterials

To investigate the off-chip photothermal effect of PB NPs and GO, the temperature changes of both suspensions were monitored during the laser irradiation process. Different concentrations of the nanomaterial suspensions (1.0 mL) in disposable UV cuvettes were horizontally exposed to the laser at a power density of 3.12 W cm^{-2} for 10 min. A digital thermometer was inserted into the suspensions to monitor the temperature change. For the further quantitative off-chip photothermal investigation, PCR tubes with different concentrations of the nanomaterial suspensions (0.1 mL) were vertically irradiated with the laser at a power density of 5.26 W cm^{-2} for 1.0 min. The temperature of the suspensions was measured by using the digital thermometer immediately after the irradiation. It should be noted that the laser irradiation intensity changed (3.12 or 5.26 W cm^{-2}) due to different laser irradiation directions and varying surface areas in different measurement situations. To study the on-chip photothermal effect of the nanomaterials, the inlets preloaded with different concentrations of the nanomaterial–dye suspensions (20 μL per well) were individually irradiated with the laser at a power density of 2.6 W cm^{-2} for different times. To record the on-chip bar-chart pumping distance, pictures of the chips were immediately taken upon the termination of the laser irradiation by using a camera (Canon EOS 600D) or a smartphone camera. The bar-chart pumping distance of the dyes was quantitatively measured by using the on-chip ruler.

On-chip transport of substances using the photothermal microfluidic pump

For on-chip (chip 2) single-sample transport, the reservoirs preloaded with different concentrations of PB NP suspensions (40 μL per well) were individually irradiated with the laser at a power density of 2.6 W cm^{-2} for different times. Pictures of the chips were immediately taken after the irradiation. The pumping time and pumping distance of the target samples from the sample wells to outlets were accurately recorded to calculate the transport rate. For the multiplexed transport chip (chip 3), the central reservoir preloaded with PB NP suspension (80 μL, 0.4 mg mL^{-1}) was irradiated for 2.0 minutes at a power density of 2.6 W cm^{-2}. The platform setup is shown in Fig. S3† including the laser and a PT-Chip.

Visual quantitative detection of PSA on the PT-Chip based on bar-chart movement distance

The procedures (see details in the ESI†) for a sandwich-type immunoassay for PSA detection and the material conversion of iron oxide NPs to PB NPs were performed according to our previously published paper.[40] Each reservoir on the PT-Chip was loaded with 30 μL of immunosensing solutions, and four reservoirs were then irradiated simultaneously under an 808 nm NIR diode laser for 5 min at a power density of 2.2 W cm^{-2}. The visual quantitative detection of PSA on the PT-Chip was achieved by simply recording the bar-chart pumping distances of the immunosensing solutions (see details in the ESI†).

Conflicts of interest

The authors declare no conflict of interest.

Acknowledgements

We would like to acknowledge the financial support from the National Institute of Allergy and Infectious Disease of the NIH (R21AI107415), the U.S. NSF (IIP 1953841 and DMR 1827745), the Philadelphia Foundation, and the Medical Center of the Americas Foundation. Financial support for our research from the National Institute of General Medical Sciences of the NIH (SC2GM105584), the NIH RCMI Pilot grant, the University of Texas (UT) System for the STARS award, and the University of Texas at El Paso (UTEP) for the IDR Program, the Multidisciplinary Research Award Program (MRAP) and the URI Program is also greatly acknowledged.

References

1 M. Dou, S. T. Sanjay, D. C. Dominguez, S. Zhan and X. Li, *Chem. Commun.*, 2017, **53**, 10886–10889.
2 M. Dou, J. M. Garcia, S. Zhan and X. Li, *Chem. Commun.*, 2016, **52**, 3470–3473.
3 M. Dou, D. C. Dominguez, X. Li, J. Sanchez and G. Scott, *Anal. Chem.*, 2014, **86**, 7978–7986.
4 P. Zuo, X. Li, D. C. Dominguez and B.-C. Ye, *Lab Chip*, 2013, **13**, 3921–3928.
5 J. Zhang, X. Wei, R. Zeng, F. Xu and X. Li, *Future Sci. OA*, 2017, **3**, FSO187.
6 S. T. Sanjay, M. Dou, G. Fu, F. Xu and X. Li, *Curr. Pharm. Biotechnol.*, 2016, **17**, 772–787.
7 Y. Ma, Y. Mao, D. Huang, Z. He, J. Yan, T. Tian, Y. Shi, Y. Song, X. Li, Z. Zhu, L. Zhou and C. J. Yang, *Lab Chip*, 2016, **16**, 3097–3104.

8 M. Dou, S. T. Sanjay, M. Benhabib, F. Xu and X. Li, *Talanta*, 2015, **145**, 43–54.
9 S. T. Sanjay, G. Fu, M. Dou, F. Xu, R. Liu, H. Qi and X. Li, *Analyst*, 2015, **140**, 7062–7081.
10 M. Dou, S. T. Sanjay, D. C. Dominguez, P. Liu, F. Xu and X. Li, *Biosens. Bioelectron.*, 2017, **87**, 865–873.
11 S. T. Sanjay, M. Dou, J. Sun and X. Li, *Sci. Rep.*, 2016, **6**, 30474.
12 M. Dou, J. Sanchez, H. Tavakoli, J. E. Gonzalez, J. Sun, J. Dien Bard and X. Li, *Anal. Chim. Acta*, 2019, **1065**, 71–78.
13 M. Dou, N. Macias, F. Shen, J. D. Bard, D. C. Dominguez and X. Li, *EClinicalMedicine*, 2019, **8**, 72–77.
14 X. J. Li and Y. Zhou, *Microfluidic Devices for Biomedical Applications*, Woodhead Publishing, 2013.
15 H. Tavakoli, W. Zhou, L. Ma, S. Perez, A. Ibarra, F. Xu, S. H. Zhan and X. J. Li, *TrAC, Trends Anal. Chem.*, 2019, **117**, 13–26.
16 S. T. Sanjay, W. Zhou, M. Dou, H. Tavakoli, L. Ma, F. Xu and X. Li, *Adv. Drug Delivery Rev.*, 2018, **128**, 3–28.
17 Y. Song, Y. Zhang, P. E. Bernard, J. M. Reuben, N. T. Ueno, R. B. Arlinghaus, Y. Zu and L. Qin, *Nat. Commun.*, 2012, **3**, 1283.
18 Y. Li, J. Xuan, Y. Song, P. Wang and L. Qin, *Lab Chip*, 2015, **15**, 3300–3306.
19 X. Wei, T. Tian, S. Jia, Z. Zhu, Y. Ma, J. Sun, Z. Lin and C. J. Yang, *Anal. Chem.*, 2016, **88**, 2345–2352.
20 X. Wei, W. Zhou, S. T. Sanjay, J. Zhang, Q. Jin, F. Xu, D. C. Dominguez and X. Li, *Anal. Chem.*, 2018, **90**, 9888–9896.
21 Y. Li, J. Xuan, T. Xia, X. Han, Y. Song, Z. Cao, X. Jiang, Y. Guo, P. Wang and L. Qin, *Anal. Chem.*, 2015, **87**, 3771–3777.
22 Z. Zhu, Z. Guan, S. Jia, Z. Lei, S. Lin, H. Zhang, Y. Ma, Z. Q. Tian and C. J. Yang, *Angew. Chem., Int. Ed.*, 2014, **53**, 12503–12507.
23 Y. Song, X. Xia, X. Wu, P. Wang and L. Qin, *Angew. Chem., Int. Ed.*, 2014, **53**, 12451–12455.
24 Y. Song, Y. Wang, W. Qi, Y. Li, J. Xuan, P. Wang and L. Qin, *Lab Chip*, 2016, **16**, 2955–2962.
25 Y. Song, Y. Wang and L. Qin, *J. Am. Chem. Soc.*, 2013, **135**, 16785–16788.
26 Y. Wang, G. Zhu, W. Qi, Y. Li and Y. Song, *Biosens. Bioelectron.*, 2016, **85**, 777–784.
27 S. K. Katla, J. Zhang, E. Castro, R. A. Bernal and X. Li, *ACS Appl. Mater. Interfaces*, 2018, **10**, 75–82.
28 X. Chen, Y. Chen, M. Yan and M. Qiu, *ACS Nano*, 2012, **6**, 2550–2557.
29 J. P. Yang, D. K. Shen, L. Zhou, W. Li, X. M. Li, C. Yao, R. Wang, A. M. El-Toni, F. Zhang and D. Y. Zhao, *Chem. Mater.*, 2013, **25**, 3030–3037.
30 P. Huang, J. Lin, W. Li, P. Rong, Z. Wang, S. Wang, X. Wang, X. Sun, M. Aronova, G. Niu, R. D. Leapman, Z. Nie and X. Chen, *Angew. Chem., Int. Ed.*, 2013, **52**, 13958–13964.
31 K. Yang, H. Xu, L. Cheng, C. Y. Sun, J. Wang and Z. Liu, *Adv. Mater.*, 2012, **24**, 5586–5592.
32 S. Fazal, A. Jayasree, S. Sasidharan, M. Koyakutty, S. V. Nair and D. Menon, *ACS Appl. Mater. Interfaces*, 2014, **6**, 8080–8089.
33 R. C. Lv, P. P. Yang, F. He, S. L. Gai, G. X. Yang and J. Lin, *Chem. Mater.*, 2015, **27**, 483–496.
34 M. Lin, D. D. Wang, S. W. Liu, T. T. Huang, B. Sun, Y. Cui, D. Q. Zhang, H. C. Sun, H. Zhang, H. Sun and B. Yang, *ACS Appl. Mater. Interfaces*, 2015, **7**, 20801–20812.
35 G. Fu, W. Liu, S. Feng and X. Yue, *Chem. Commun.*, 2012, **48**, 11567–11569.
36 G. Fu, W. Liu, Y. Li, Y. Jin, L. Jiang, X. Liang, S. Feng and Z. Dai, *Bioconjugate Chem.*, 2014, **25**, 1655–1663.
37 H. K. Moon, S. H. Lee and H. C. Choi, *ACS Nano*, 2009, **3**, 3707–3713.
38 H. T. Ke, J. R. Wang, Z. F. Dai, Y. S. Jin, E. Z. Qu, Z. W. Xing, C. X. Guo, X. L. Yue and J. B. Liu, *Angew. Chem., Int. Ed.*, 2011, **50**, 3017–3021.
39 X. D. Li, X. L. Liang, F. Ma, L. J. Jing, L. Lin, Y. B. Yang, S. S. Feng, G. L. Fu, X. L. Yue and Z. F. Dai, *Colloids Surf., B*, 2014, **123**, 629–638.
40 G. Fu, S. T. Sanjay, M. Dou and X. Li, *Nanoscale*, 2016, **8**, 5422–5427.
41 G. Fu, S. T. Sanjay, W. Zhou, R. A. Brekken, R. A. Kirken and X. Li, *Anal. Chem.*, 2018, **90**, 5930–5937.
42 J. Zhang, H. Xing and Y. Lu, *Chem. Sci.*, 2018, **9**, 3906–3910.
43 W. Zhou, K. Hu, S. Kwee, L. Tang, Z. Wang, J. Xia and X. Li, *Anal. Chem.*, 2020, **92**, 2739–2747.
44 M. C. Wu, A. R. Deokar, J. H. Liao, P. Y. Shih and Y. C. Ling, *ACS Nano*, 2013, **7**, 1281–1290.
45 J. T. Robinson, S. M. Tabakman, Y. Liang, H. Wang, H. S. Casalongue, D. Vinh and H. Dai, *J. Am. Chem. Soc.*, 2011, **133**, 6825–6831.
46 G. Fu, S. T. Sanjay and X. Li, *Analyst*, 2016, **141**, 3883–3889.
47 P. Marmottant and S. Hilgenfeldt, *Proc. Natl. Acad. Sci. U. S. A.*, 2004, **101**, 9523–9527.
48 H. Obata, T. Kuji, K. Kojima, F. Sassa, M. Yokokawa, K. Takekosh and H. Suzuki, *ACS Sens.*, 2016, **1**, 190–196.
49 R. H. Lahr, G. C. Wallace and P. J. Vikesland, *ACS Appl. Mater. Interfaces*, 2015, **7**, 9139–9146.
50 X. Jiang, C. Sun, Y. Guo, G. Nie and L. Xu, *Biosens. Bioelectron.*, 2015, **64**, 165–170.
51 Y. J. Long, Y. F. Li, Y. Liu, J. J. Zheng, J. Tang and C. Z. Huang, *Chem. Commun.*, 2011, **47**, 11939–11941.
52 X. X. Wang, Q. Wu, Z. Shan and Q. M. Huang, *Biosens. Bioelectron.*, 2011, **26**, 3614–3619.
53 Z. Li, H. Chen and P. Wang, *Analyst*, 2019, **144**, 3314–3322.
54 M. Shokouhimehr, E. S. Soehnlen, J. H. Hao, M. Griswold, C. Flask, X. D. Fan, J. P. Basilion, S. Basu and S. P. D. Huang, *J. Mater. Chem.*, 2010, **20**, 5251–5259.
55 M. Shokouhimehr, E. S. Soehnlen, A. Khitrin, S. Basu and S. P. D. Huang, *Inorg. Chem. Commun.*, 2010, **13**, 58–61.

Electronic Supplementary Material (ESI) for Lab on a Chip.
This journal is © The Royal Society of Chemistry 2019

Supporting Information

Remotely tunable microfluidic platform driven by nanomaterial-mediated on-demand photothermal pumping

Guanglei Fu, ‡ [a,b] Wan Zhou, ‡ [a] and XiuJun Li *[a,c,d,e]

[a] *Department of Chemistry and Biochemistry, University of Texas at El Paso, 500 West University Ave, El Paso, Texas, 79968, USA.*

[b] *Biomedical Engineering Research Center, Medical School of Ningbo University, Ningbo, Zhejiang, 315211, P. R. China*

[c] *Biomedical Engineering, University of Texas at El Paso, 500 West University Ave, El Paso, Texas, 79968, USA.*

[d] *Border Biomedical Research Center, University of Texas at El Paso, 500 West University Ave, El Paso, Texas, 79968, USA.*

[e] *Environmental Science and Engineering, University of Texas at El Paso, 500 West University Ave, El Paso, Texas, 79968, USA.*

*Corresponding author: XiuJun Li, xli4@utep.edu

‡These authors contributed equally to the work

Additional Experimental Details

Synthesis of Fe_3O_4 NPs-secondary antibody conjugates

The Fe_3O_4 NPs-secondary antibody conjugates were synthesized as per previously published protocols with slight modification.[1,2] Basically, *N*-hydroxysulfosuccinimide (Sulfo-NHS, 25 mg/mL) and 1-ethyl-3-[3-dimethylaminopropyl]carbodiimide hydrochloride (EDC·HCl, 30 mg/mL) were added to the Fe_3O_4 NPs dispersion (0.25 mg/mL), followed by reaction at room temperature for 40 min. Then 40 μg of polyclonal PSA secondary antibody was added into the nanoparticle dispersion, and reacted for 2 h on an orbital shaker. The nanoparticle dispersion was centrifuged at 12,000 rpm for 10 min and washed with phosphate buffer saline (PBS, pH 7.4, 0.01 M) three times. The as-produced Fe_3O_4 NPs-secondary antibody conjugates were dispersed in 1 mL PBS buffer and stored at 4 °C before use.

Immunosensing procedures

In a typical sandwich enzyme-linked immunosorbent assay (ELISA), 120 μL of monoclonal PSA primary antibody (30 μg/mL) was added in a PCR tube, followed by overnight incubation at 4 °C. After washing the tube with PBS buffer for three times, 200 μL of 5% BSA was added and incubated for 30 min at 37 °C in order to block remaining active sites. Then 120 μL of PSA solutions with different concentrations from 0 to 64 $ng \cdot mL^{-1}$ were added to each tube and incubated for 1 h at 37 °C, followed by washing steps. 120 μL of freshly synthesized Fe_3O_4 NPs-secondary antibody conjugates were added and incubated at 37 °C for 1 h, after which the tube was washed thoroughly with PBS buffer.

Nanoparticles transformation

According to the previous work published from our group,[1,2] a weak photothermal agent, Fe_3O_4 NPs (captured in the sandwich immunoassay system), was herein transformed into a strong photothermal agent, Prussian blue (PB) NPs. Briefly, 120 μL of HCl solution (0.1 M) was added into the above tube, followed by ultrasonication for 1 h at room temperature. Potassium ferrocyanide aqueous solutions (30 μL, 90 mM) were then added into each tube, followed by vigorous mixing for 1 h. Finally, the PB NPs were produced via the ferric ferricyanide reaction under acidic conditions.

Visual quantitative immunosensing using the PT-Chip

The above PB NPs captured in the immunoassay were pipetted to the photothermal bar-chart chip (PT-Chip) for visual quantitative detection of PSA. In detail, 30 μL of the above solution was loaded into each reservoir on the PT-Chip, along with 2 μL of food dye solution (a deep blue color for better observation of bar chart movement). All reservoirs on a single chip were then irradiated simultaneously under an 808 nm NIR diode laser at a power density of 2.2 $W \cdot cm^{-2}$. With the increasing heat generated under the laser irradiation (up to 5 min), vapor pressure accumulated inside the PT-Chip,

which pumped the solutions to microchannels and displayed bar chart movement. Therefore, the visual quantitative detection of PSA was achieved by simply recording the bar-chart pumping distances of the immunosensing solutions, which were conveniently read by using an on-chip ruler from the PT-Chip.

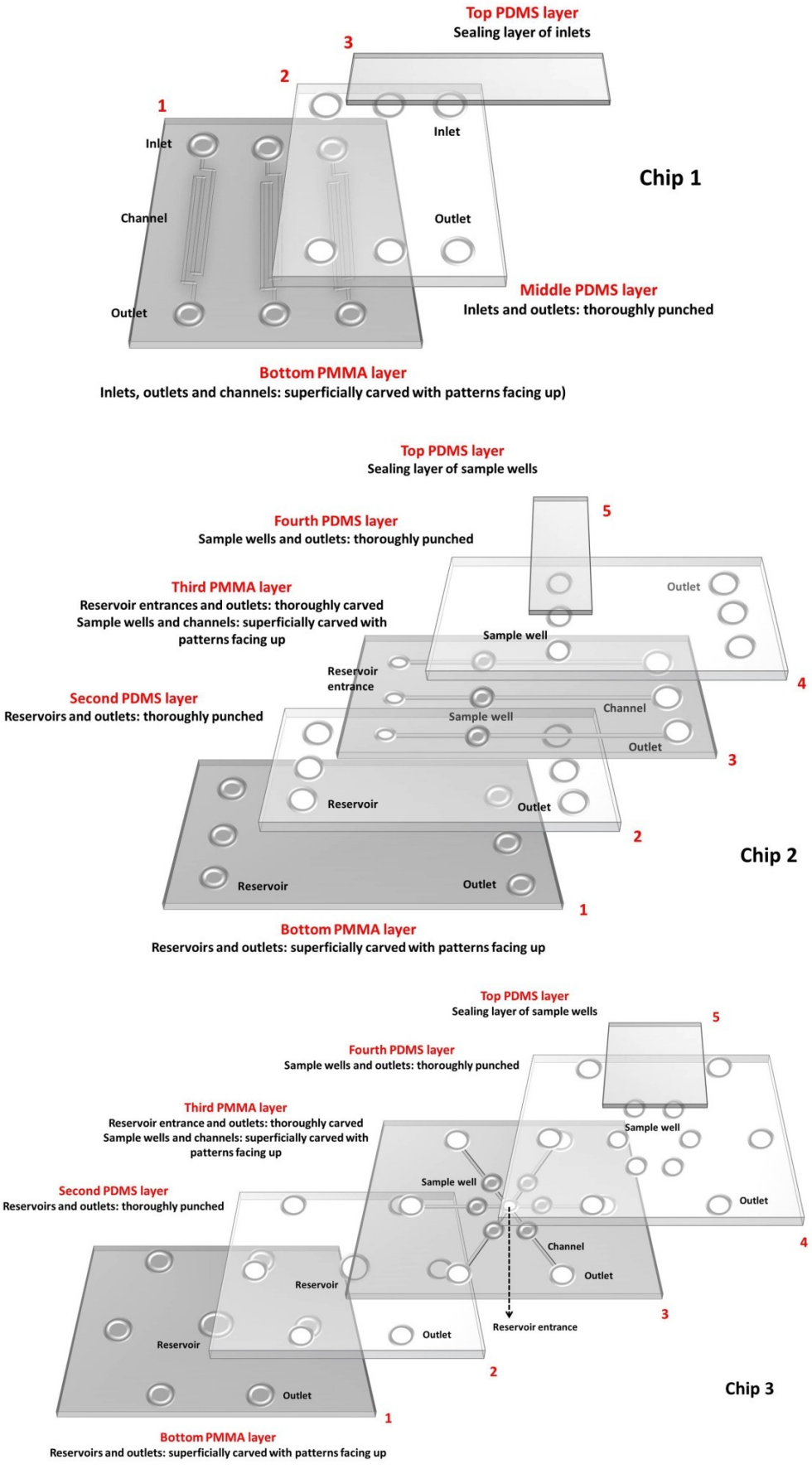

Figure S1. Schematic illustration of structures of **Chip 1**, **Chip 2**, and **Chip 3**.

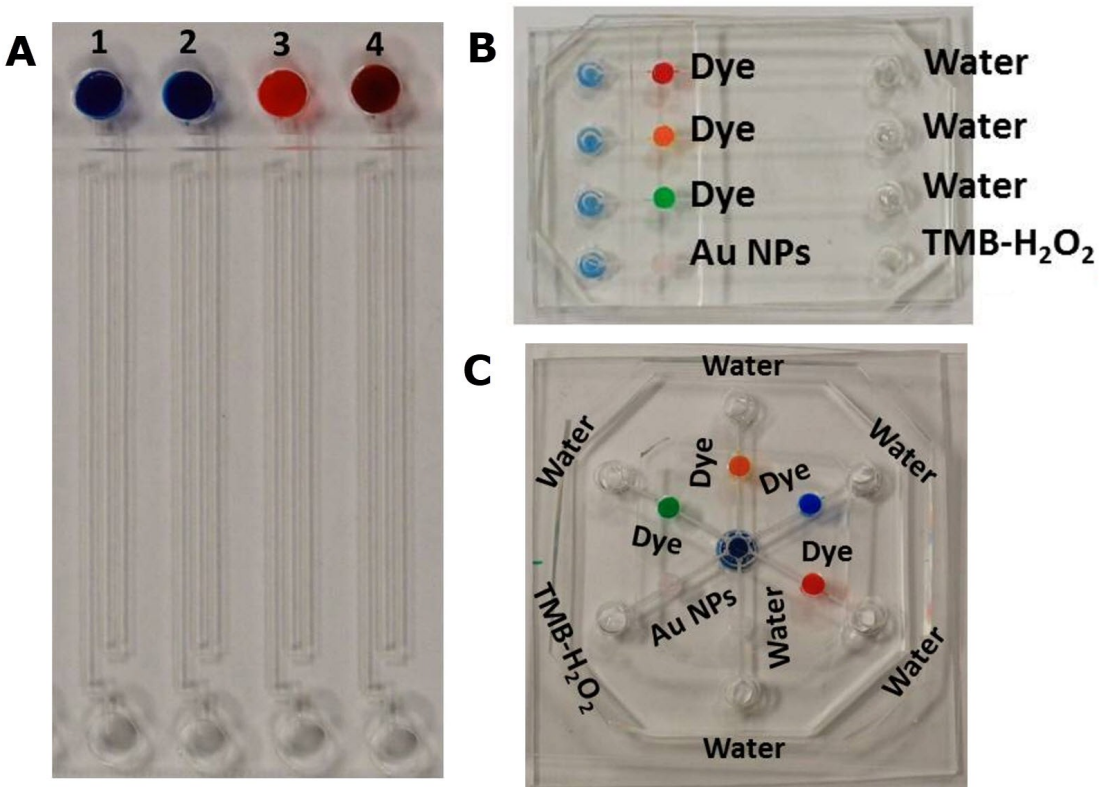

Figure S2. Photographs of (A) **Chip 1**, (B) **Chip 2**, and (C) **Chip 3**.

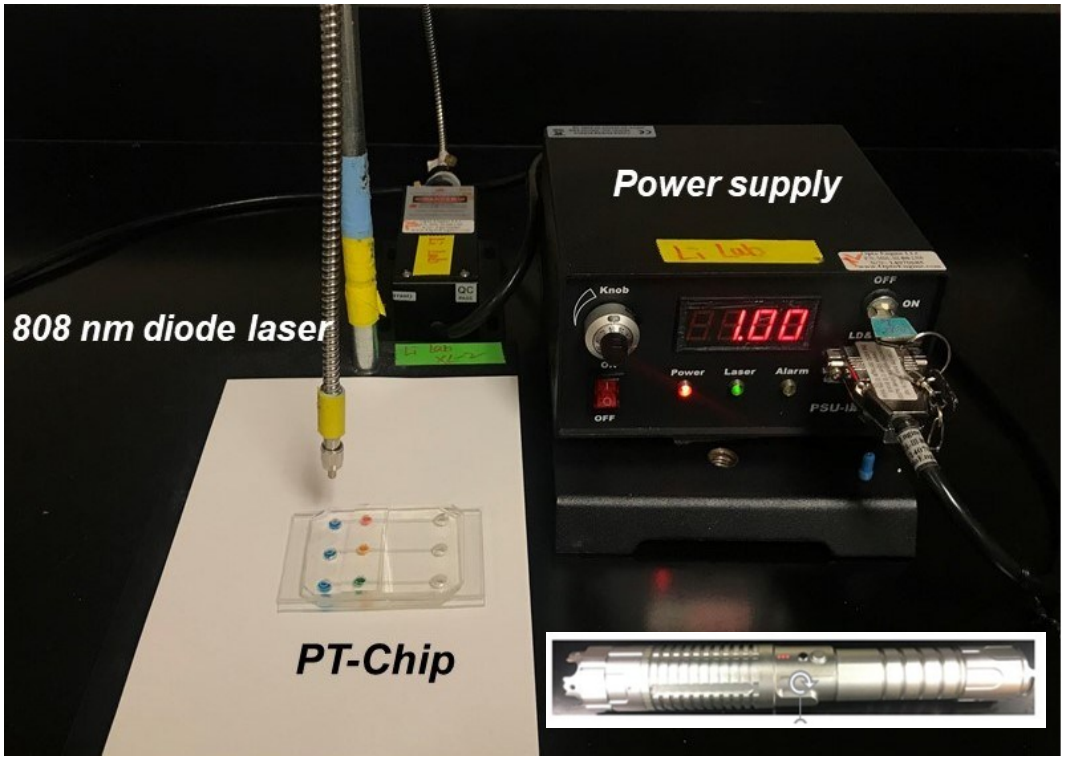
808 nm diode laser
Power supply
Knob
1.00
Power
Laser
Alarm
OFF
ON
PT-Chip

Figure S3. Photograph of the platform setup including the laser and the PT-Chip. The inset is a NIR laser pointer.

References

1. G. Fu, S. T. Sanjay, W. Zhou, R. A. Brekken, R. A. Kirken and X. Li, *Anal. Chem.*, 2018, **90**, 5930-5937.
2. G. L. Fu, S. T. Sanjay, M. W. Dou and X. J. Li, *Nanoscale*, 2016, **8**, 5422-5427.